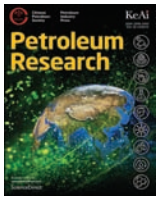
Petroleum Research 11 (2026) 870–879

Contents lists available at ScienceDirect

Petroleum Research

journal homepage: http://www.keaipublishing.com/en/journals/petroleum-research/



Full Length Article

Study on the phase behavior and mass transfer laws of CO_2-shale oil in shale oil reservoirs

FuLin Yang [a,b,*], YingYing Chen [a,b]

[a] Guangxi Key Laboratory of Green Chemical Materials and Safety Technology, Beibu Gulf University, Qinzhou, Guangxi 535011, China
[b] College of Petroleum and Chemical Engineering, Beibu Gulf University, Qinzhou, Guangxi 535011, China

ARTICLE INFO

Article history:
Received 19 May 2025
Received in revised form
19 November 2025
Accepted 21 November 2025
Available online 1 December 2025

Keywords:
Vapor-liquid phase equilibrium
Nanoconfinement effect
Phase behavior
Mass transfer
Geological storage

ABSTRACT

Injecting CO_2 into shale oil reservoirs has the dual purpose of enhancing oil recovery rate and geological storage of CO_2. The phase behavior and mass transfer laws of the CO_2-shale oil are crucial for achieving highly efficient production shale oil and gas. Based on an improved vapor-liquid equilibrium (VLE) model in nanopores, which achieves a relative error of less than 3.16%, this study investigates the phase behavior and CO_2–oil mass transfer laws of two representative shale oils under CO_2 injection. Research results show that after CO_2 injection, the saturation pressure tends first to increase and then reduce. The CO_2 dissolution results in a significant reduction in the molecular weight and viscosity of Wolfcamp shale oil. During the multi-contact shale oil with CO_2 injection, both density and the interfacial tension (IFT) reduce at the forward contact edge, indicating forward-contact miscibility. Furthermore, the nanoconfinement effect reduces the density difference between the liquid and gas phases, leading to a reduction in the IFT, which is beneficial for gas-oil miscibility. The study results can provide a theoretical basis for understanding compositional variations in shale oils under CO_2 injection, offering promising improvements in miscibility and recovery efficiency.

© 2025 Chinese Petroleum Society. Publishing services by Elsevier B.V. on behalf of KeAi Communications Co. Ltd. This is an open access article under the CC BY-NC-ND license (http://creativecommons.org/licenses/by-nc-nd/4.0/).

1. Introduction

In recent years, unconventional reservoirs, such as shale and tight oil reservoirs, have emerged as a key area for the exploration and development of oil and gas (Dordzie et al., 2025; Rui et al., 2025). CO_2 injection into shale reservoirs enhances oil recovery (EOR) and stores CO_2 in shale oil reservoirs (Li et al., 2025). In shale oil reservoirs, the pore size distribution generally ranges from 1 to 100 nm (Song et al., 2021). Due to the nanoconfinement effects generated by these nanopores, the fluid's phase behavior within the nanopore deviates significantly from that of the bulk phase (Mohagheghian et al., 2020). The phase behavior is of critical importance for the optimization of development strategies and reserve prediction. Therefore, accurately describing the CO_2-shale oil phase behavior in nanopores is crucial for highly efficient production in shale reservoirs.

Through experimental methods such as the nanofluidic device (Wang et al., 2024) and adsorption-desorption experiments (Liu et al., 2019), some scholars have observed that hydrocarbons in nanopores have a lower critical temperature and pressure than those in the bulk phase, and this difference is progressively growing as the pore size decreases (Liu et al., 2019; Salahshoor et al., 2017; Tan et al., 2019). Experimental measurements are often considered the most straightforward method for studying the phase behavior of confined fluids. However, due to the nature of shale formations and equipment limitations, such as the difficulty of constructing a nanochannel or high-quality nanoporous medium, experimental measurements are challenging, and the precision of the obtained data suffers from uncertainties (Song et al., 2021). Due to the limitations of experimental methods, theoretical approaches, including equation of state (EOS) modelling (Song et al., 2021), density functional theory (DFT) (Zhao et al., 2019), and molecular simulation (MS) (Dong et al., 2023; Liu et al., 2025) have been applied extensively. The DFT and MS can provide more detailed insights into the phase behavior of fluids in nanopores (Liu et al., 2019). However, as system scale and fluid complexity increase slightly, the DFT and MS calculations may

* Corresponding author. Guangxi Key Laboratory of Green Chemical Materials and Safety Technology, Beibu Gulf University, Qinzhou, Guangxi 535011, China
E-mail address: fulinyang@sina.com (F. Yang).
Peer review under the responsibility of Editorial Office of Petroleum Research.

https://doi.org/10.1016/j.ptlrs.2025.11.005
2096-2495/© 2025 Chinese Petroleum Society. Publishing services by Elsevier B.V. on behalf of KeAi Communications Co. Ltd. This is an open access article under the CC BY-NC-ND license (http://creativecommons.org/licenses/by-nc-nd/4.0/).

require significant computational expense and an estimate with higher accuracy, which restricts their application at the reservoir or core scale (Liu et al., 2019). The EOS models are currently used in commercial simulation software and considered as one of the most promising approaches for reservoir scale.

Considering capillary pressure in the EOS model, Brusilovsky (1992) first calculated vapor-liquid equilibrium (VLE) for hydrocarbon mixtures in porous media. Due to the existing capillary pressure, the dew point and bubble point pressures are higher and lower, respectively, than those in the bulk state. In the following years, numerous studies have found that capillary pressure in nanopores has a significant impact on the VLE (Abu et al., 1999; Hamada et al., 2007; Tan et al., 2017). Nojabaei et al. (2013) demonstrated that the two-phase envelope in a confined space deviates significantly from that of the bulk phase due to the capillary pressure. They also observed that the dew point pressure increased in the upper part of the dew point pressure but decreased in the lower part of the dew point pressure. Additionally, due to the zero capillary pressure at the critical point, the VLE at the critical point was unaffected by the nanopore. The above findings are in agreement with Sandoval et al. (2015). Rezaveisi et al. (2018) coupled capillary pressure in the EOS model and found that each temperature has a maximum capillary pressure, above which the VLE is impossible. To improve the calculation accuracy of VLE in nanopores, many scholars have considered the effect of shifted critical properties in the EOS model. In addition, Zhang et al. (2019) improved the van der Waals equation of state (vdW-EOS) by taking into account the effects of pore walls and intermolecular interactions. The Peng-Robinson equation of state (PR-EOS) was extended by Luo et al. (2019) using the fluid-pore interaction parameters, and the model predicted the phase transition temperatures of the confined fluids at different pore sizes. Yang et al. (2019) extended the PR-EOS by coupling the capillary pressure and critical property shifts. Song et al. (2020a) suggested a novel adsorption PR-EOS (A-PR-EOS). Based on this A-PR-EOS, they investigated the relationship between fluid adsorption and the critical point shifts it causes in pure components. However, most studies have focused on the phase behavior of pure hydrocarbon mixtures, and few studies have been conducted on the phase behavior of CO_2-shale oil affected by nanoconfinement effects.

To the best of our knowledge, the nanoconfinement effect on the phase behavior of CO_2-shale oil under high CO_2 concentration has not been reported in the literature. In this study, a VLE thermodynamic model considering the nanoconfinement effect is first proposed based on capillary pressure and shifts in critical properties. Literature cases then verify the accuracy of the improved VLE algorithm. Secondly, taking the typical Eagle Ford and Wolfcamp shale oil as the research objects, the characteristics of fluid phase behavior after CO_2 injection are elucidated, and the dynamic change characteristics of parameters such as fluid composition, interfacial tension (IFT), and density during the multiple oil and gas contacts process after CO_2 injection are clarified. Finally, the changes in the rules phase behaviors (e.g., vapor-liquid phase density, IFT, and capillary force) of shale oil in the nanopores are explored. The injection CO_2 concentration ranges from 0 to 99.8 mol%. The study results can provide an important theoretical framework to support the production of unconventional resources.

2. Proposed vapor-liquid equilibrium (VLE) algorithm

2.1. VLE modeling

In this study, a modified PR-EOS (Abudour et al., 2013) is employed to predict the VLE in confined spaces. A critical point shift model and the capillary pressure are coupled with PR-EOS to reflect the effects of confinement yielded by nanopores. For a given pressure, temperature, and mixture composition, the gas-liquid equilibrium (VLE) criterion is that the fugacity ratio of each component in the gas and liquid phases is equal to 1, as shown in Eq. (1) (Wei et al., 2022).

$$\frac{f_i^L}{f_i^V} = \frac{x_i \phi_i^{\mathrm{L}} P_{\mathrm{L}}}{y_i \phi_i^{\mathrm{V}} P_{\mathrm{V}}} = 1, i = 1, \ldots, N_c \tag{1}$$

Where f_i^V is the fugacity of component i in the gas phase; f_i^L is the fugacity of component i in the liquid phase; $\varnothing_i^L$ is the fugacity coefficient of component i in the liquid phase; $\varnothing_i^V$ is the fugacity coefficient of component i in the gas phase; P_{L} is the pressure of the liquid phase, 10^{-1}MPa; P_{V} is the pressure of the gas phase, 10^{-1}MPa.

The component fugacities can be calculated by the Eqs. (2) and (3):

$$\ln \frac{f_i^V}{y_i P_V} = \ln \varphi_i^V = \frac{B_i}{B_V}(Z_V - 1) - \ln(Z_V - B_V) + \frac{A_V}{2\sqrt{2}B_V}\left[\frac{B_i}{B_V} - \frac{2}{A_V}\sum_{j=1}^{N_c} y_i A_{ij}\right] \ln\left(\frac{Z_V + \left(1+\sqrt{2}\right)B_V}{Z_V + \left(1-\sqrt{2}\right)B_V}\right), i, j = 1, \ldots, Nc \tag{2}$$

$$\ln \frac{f_i^L}{x_i P_L} = \ln \varphi_i^L = \frac{B_i}{B_L}(Z_L - 1) - \ln(Z_L - B_L) + \frac{A_L}{2\sqrt{2}B_L}\left[\frac{B_i}{B_L} - \frac{2}{A_L}\sum_{j=1}^{N_c} x_i A_{ij}\right] \ln\left(\frac{Z_L + \left(1+\sqrt{2}\right)B_L}{Z_L + \left(1-\sqrt{2}\right)B_L}\right), i, j = 1, \ldots, N_C \tag{3}$$

Where A and B are EOS constants; Z_L is the liquid-phase compressibility factor; Z_V is the gas-phase compressibility factor; x_i is the molar fraction of component i in the liquid phase; y_i is the molar fraction of component i in the gas phase; N_c is the total number of components in the mixture system.

Due to the presence of capillary pressure in nanopores, the pressures of the liquid phase and the vapor phase cannot be assumed to be equal. Assuming that the liquid phase is the non-wetted phase and the vapor phase is the wetted phase. The capillary pressure versus vapor-liquid phase pressure in nanopores is given in Eq. (4):

$$P_{cap} = P_V - P_L \tag{4}$$

Where P_{cap} is the capillary pressure, 10^{-1}MPa.

The capillary pressure is calculated using the Young-Laplace equation (Adamson, 1990), assuming equal pore radius:

$$P_{cap} = \frac{2\sigma \cos\theta}{r_p} \tag{5}$$

Where σ is the gas-liquid IFT, mN/m; θ is the contact angle, °. According to the results of literature experiments (Zhang et al., 2017), θ is assumed to be 30°.

The gas-liquid IFT is calculated using the Macleod-Sugden equation (Wei et al., 2022) as shown in Eq. (6):

$$\sigma = \left[\sum_{i=1}^{N_c} P_{chi}(x_i\rho_L - y_i\rho_V)\right]^4, i = 1, \ldots, N_c \tag{6}$$

Where P_{chi} is the Parachor constant of component i; ρ_L is the liquid phase density, mol/cm^3; ρ_V is the gas phase density, mol/cm^3.

In addition to the capillary pressure, the critical property shift also affects the phase behavior within the nanopore. The critical property shift model by Zarragoicoechea and Kuz (2004) can only be applied to the range of $\sigma_{LJ}/\ r_p \leqq 0.37$ (Li et al., 2017; Teklu et al., 2014). For the largest molecule of Eagle Ford shale oil, C_{13}–C_{21}, the calculated σ_{LJ} value is 0.902 nm, so the minimum pore radius should be 2.44 nm. In this study, a critical property shift model, as suggested by Ma et al. (2013), is used. The model is as follows:

$$\frac{T_{cb} - T_{cp}}{T_{cb}} = 1.1775\left(\frac{\sigma_{LJ}}{r_p}\right)^{-1.338} \quad for \quad \left(\frac{\sigma_{LJ}}{r_p}\right) \geq 1.5 \tag{7}$$

$$\frac{T_{cb} - T_{cp}}{T_{cb}} = 0.6 \quad for \quad \left(\frac{\sigma_{LJ}}{r_p}\right) < 1.5 \tag{8}$$

$$\frac{P_{cb} - P_{cp}}{P_{cb}} = 1.5686\left(\frac{\sigma_{LJ}}{r_p}\right)^{-0.783} \tag{9}$$

$$\sigma_{LJ} = 0.244\sqrt[3]{\frac{T_{cb}}{P_{cb}}} \tag{10}$$

Where P_{cb} is the bulk phase critical temperature, K; T_{cp} is the pore critical temperature, K; P_{cap} is the capillary pressure, 10^{-1}MPa; P_{cb} is the bulk phase critical pressure, 10^{-1}MPa; σ_{LJ} is the Lennard-Jones collision diameter, nm; r_p is the pore radius, nm.

Before the VLE calculation, the gas-liquid equilibrium constant K_i for each component is initialized by Wilson's equation:

$$K_i = \frac{P_{ci}}{P}\exp\left[5.373(1+\omega_i)\left(1 - \frac{T_{ci}}{T}\right)\right] \tag{11}$$

Where P is the reservoir pressure, 10^{-1} MPa; T is the reservoir temperature, K; T_{ci} is the critical temperature of component i, K; P_{ci} is the critical pressure of component i, 10^{-1} MPa; ω_i is the eccentric factor of component i.

After initializing K_i, K_i is used to solve the Rachford-Rice equation for the compositions of the gas-liquid phase and the phase mole fraction. The Rachford-Rice equation is expressed in Eq. (12):

$$\sum_{i=1}^{N_c}(y_i - x_i) = \sum_{i=1}^{N_c}\left(\frac{(K_i - 1)Z_i}{1 + F_v(K_i - 1)}\right) = 0, i = 1, \ldots, N_c \tag{12}$$

Where: F_V is the gas fraction of the i component of the mixture; Z_i is the total molar fraction of component i in the mixture.

The obtained phase mole fraction and the phase compositions are used to examine the VLE criterion with an error tolerance of 10^{-6}. If the VLE criterion is reached, then the calculation stops. If the VLE criterion cannot be satisfied, K_i is updated using Eq. (13), and the above procedure is repeated until the VLE criterion is met.

$$K_i^{(n+1)} = \frac{f_i^{L(n)}}{f_i^{V(n)}}K_i^{(n)} = \left(\frac{x_i\phi_i^L P_L}{y_i\phi_i^V P_V}\right)^{(n)} K_i^{(n)}, i = 1, \ldots, N_c \tag{13}$$

Where K_i is the gas-liquid equilibrium constant of component i at phase equilibrium; n is the number of iterations.

The gas-liquid phase equilibrium (VLE) is calculated using the Newton-Raphson iteration method based on the improved PR-EOS. The flowchart of the modified VLE algorithm is shown in Fig. 1.

2.2. VLE model validation

In this section, the bubble point pressure data of the Bakken shale oil system (T = 116.1 °C) are taken from the literature (Teklu

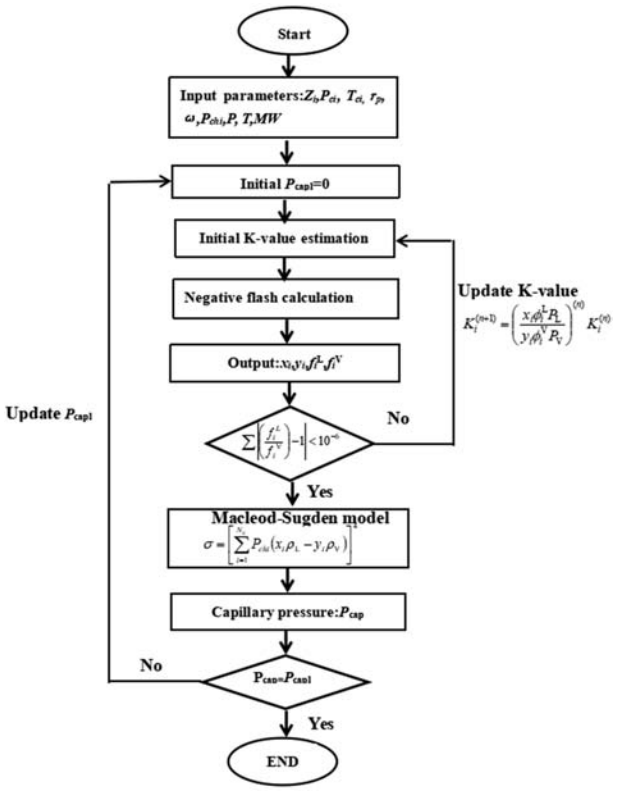


Fig. 1. Flowchart of the VLE algorithm.

et al., 2014). The VLE model developed in this study is used to predict the bubble point pressure for the Bakken shale oil. The predicted values are compared with the literature data in Fig. 2. It is found that the modified VLE model can accurately predict the phase behavior of the Bakken shale oil in both the bulk phase and nanopore, yielding excellent results that are in agreement with the literature data (Teklu et al., 2014). Under the conditions of $r_p = 1000$ nm, the established VLE model is used to predict the gas-liquid density of the quaternary system (80 mol% CO_2, 5 mol% CH_4, 6 mol% n-C_4H_{10} and 9 mol% n-$C_{10}H_{22}$) (Song et al., 2020b). The calculated results are shown in Fig. 3. As can be seen from Fig. 3, the relative error between the calculated values and the experimental result is less than 3.16 % (the average error is 1.48%), indicating that the proposed VLE model can accurately predict the VLE in nanopores.

3. Results and discussion

3.1. Shale oil used in this study

In this study, two typical shale oil samples from the literature (Li et al., 2017; Yang et al., 2019), namely Wolfcamp shale oil (WC) and Eagle Ford shale oil (EF), are selected. The fluid parameters of Wolfcamp shale oil and Eagle Ford shale oil are listed in Tables 1 and 2. As shown in Tables 1 and 2, EF shale oil is characterized by a high methane content (58.16 mol%) and a relatively low C_7^+ content (22.63 mol%). The WC shale oil has a relatively low methane content (33.838 mol%) and a relatively high C_7^+ content (32.84 mol%). According to the triangular phase diagram method (Song et al., 2024), EF shale oil is classified as high-volatile oil, while WC shale oil is categorized as light black oil.

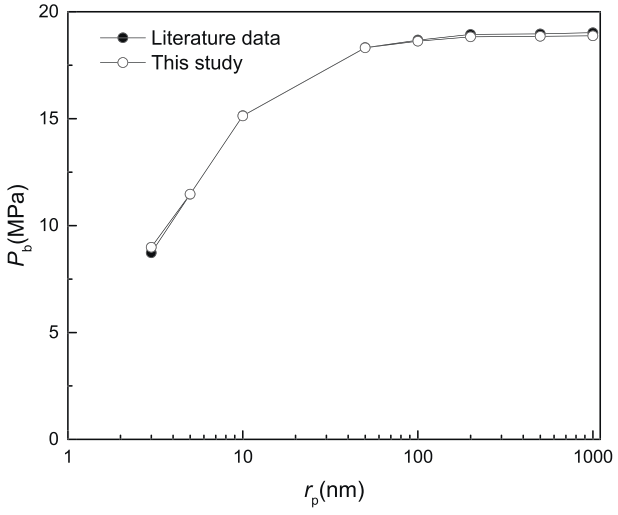


Fig. 2. Comparison of improved VLE model predicted value with literature results (Teklu et al., 2014).

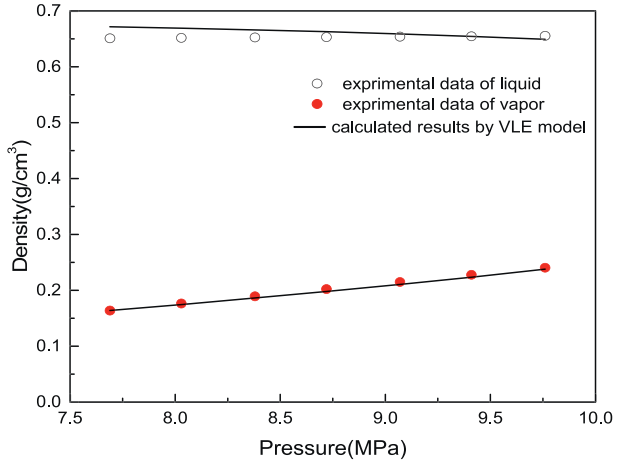


Fig. 3. Comparison of the improved VLE model predicted value with literature results.

3.2. Physical properties of shale oil after CO_2 injection

Under the conditions of $r_p = 1000$ nm, based on the VLE model, studies are conducted to investigate the effect of CO_2 content (0–99.8 mol%) in shale oil on physical properties, including viscosity, saturation pressure, molecular weight, and density. The results are shown in Fig. 4. As shown in Fig. 4, with the CO_2 content increasing, the saturation pressure first increase and then decreases, exhibiting a greater change for WC shale oil (Fig. 4a). The saturation pressure of the EF and WC shale oils changes from bubble point pressure to dew point pressure, with critical points at 29.60 MPa (59.2 mol% CO_2) and 31.89 MPa (73.4 mol% CO_2), respectively (Fig. 4a). The molecular weight shows a "linear" decline trend. The bigger the initial molecular weight is, the larger the decreasing rate and magnitude are. When CO_2 content is 99.8 mol%, the molecular weights of EF and WC shale oils are 44.15 and 44.47, respectively, which is closer to the molecular weight of pure CO_2 (Fig. 4b). This indicates the influence of CO_2 on lightning in shale oils, particularly significant for oils with bigger initial molecular weights.

Due to a change in the composition of shale oil after CO_2 injection, the density, viscosity, molar volume, and expansion coefficient are changed. As CO_2 content increases, the density of the EF and WC shale oils first increases, reaches the maximum value, and then decreases rapidly. When CO_2 content exceeds 80 mol%, the density of EF reduces rapidly due to the CO_2 dissolution effect (Fig. 4c). With the increase in CO_2 concentration, the molar volume decreases and then increases (Fig. 4d), which is due to the closer molecular arrangement of the mixture after the injection of CO_2. As the CO_2 content rises, the continuous expansion coefficient increases. The expansion behavior becomes more pronounced when CO_2 content exceeds 60 mol%. The EF shale oil with higher light component content shows a better expansion behavior from CO_2 dissolution (Fig. 4e). The viscosity decreases as the CO_2 mole content increases. The reduced viscosity of WC shale oil with higher heavy component content is more than that of EF shale oil at the same CO_2 level (Fig. 4f). This highlights that CO_2 dissolution can reduce viscosity, facilitate fluid flow, and improve recovery efficiency in shale oil reservoirs.

To further analyze the reasons for the changes in saturated pressure, the P-T phase diagram was calculated for different CO_2 contents (see Fig. 5). As shown in Fig. 5, as CO_2 content increases, the phase envelopes of the MC and EF shale oils first shift upward and then gradually shift downward, exhibiting a shrinking trend.

Table 1
Fluid parameters for Eagle Ford Shale oil (Yang et al., 2019).

	C_1	C_2	C_3	C_4	CO_2	C_5–C_6	C_7–C_{12}	C_{13}–C_{21}
Z_i, %	58.16	7.44	4.17	2.59	2.32	2.69	13.21	9.42
MW	16.04	30.07	44.10	58.12	44.01	76.502	122.96	255.28
T_c,K	190.56	305.33	369.83	418.71	304.21	485.60	606.69	778.31
P_c, MPa	4.5988	4.8718	4.2479	3.7383	7.3739	3.3767	2.7083	1.5598
ω	0.0110	0.0990	0.1520	0.1948	0.2250	0.2398	0.3548	0.7408
P_{chi}	74.05	112.91	154.03	189.30	82.00	247.57	402.33	834.82

Table 2
Fluid parameters for Wolfcamp shale oil (Li et al., 2017; Yang et al., 2019).

	C_1	C_2	C_3	C_4	C_5–C_6	C_7–C_{12}	C_{13}–C_{21}	C_{22}–C_{80}
Z_i, %	33.838	8.797	9.693	6.014	8.818	18.931	7.689	6.220
MW	16.535	30.433	44.097	58.124	78.295	120.562	220.716	443.513
T_c,K	186.30	305.54	369.98	421.78	486.38	585.14	740.05	1046.94
P_c, MPa	4.516	4.978	4.246	3.768	3.180	2.505	1.721	1.311
ω	0.0102	0.1028	0.1520	0.1894	0.2684	0.4291	0.7203	1.0159
P_{chi}	74.8	107.7	151.9	189.6	250.2	350.2	590.0	1216.8

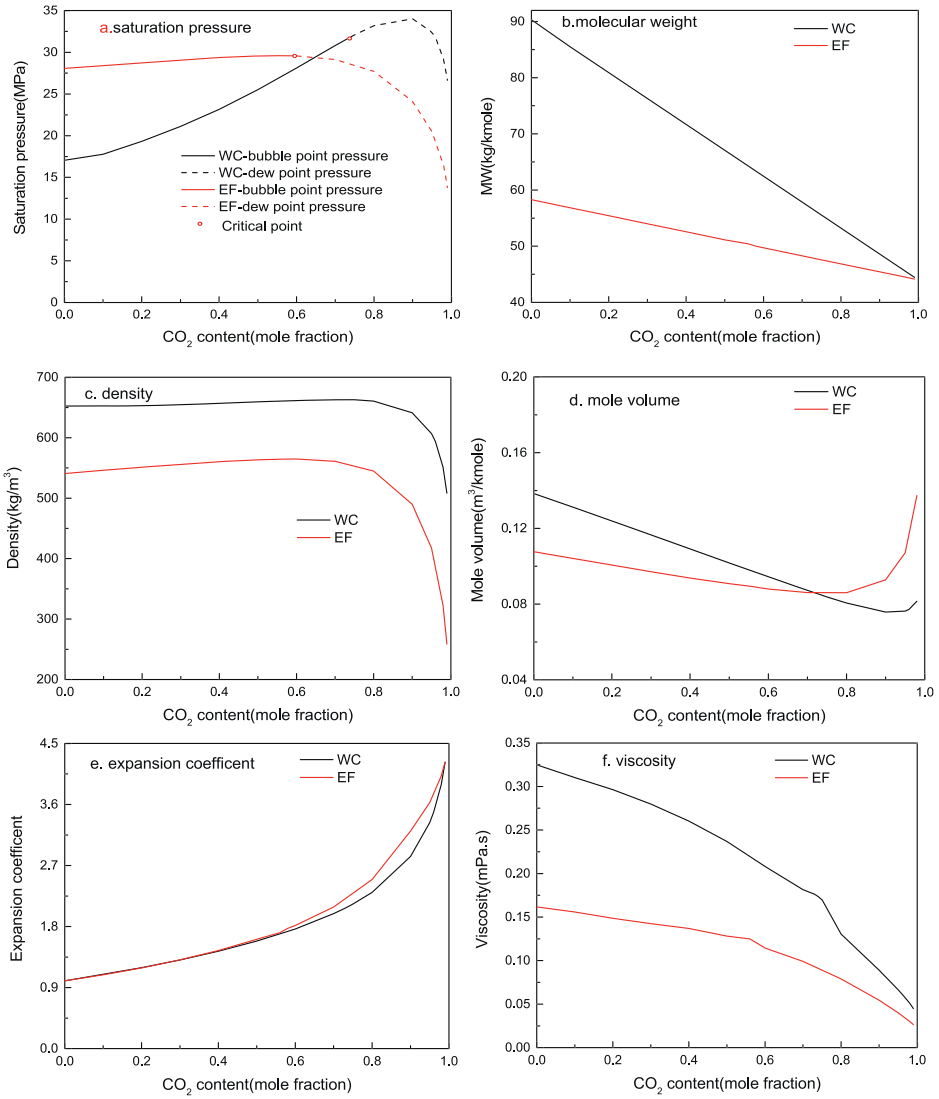


Fig. 4. Effect of CO_2 content in WC and EF shale oils on physical properties.

This indicates that as CO_2 is injected, the molecular arrangement of the mixture becomes more compact.

3.3. Phase behavior of fluid during the multi-contact CO_2-shale oil process

When CO_2 is injected into a shale reservoir, CO_2 repeatedly contacts shale oil, and the components are mass-transferred in situ between the oil and gas phases, resulting in multiple contact gas-oil miscibility. This process can be divided into two parts: forward contact and backward contact. At the leading edge of the miscible transition zone, forward contact occurs, changing the composition of the vapor phase when the equilibrium gas phase comes into contact with fresh oil. At the trailing edge of the miscible transition zone, backward contact occurs, altering the composition of the oil phase as the oil phase (residual oil) comes into contact with newly injected CO_2. Under the conditions of $r_p = 1000$ nm, P = 20 MPa and CO_2 injected amount = 30 mol%, using the modified VLE model, it is carried out on changes in fluid composition, density, and IFT with an increase of contact times for EF and WC shale oils (shown in Fig. 6). To facilitate comparison and analysis, the intermediate hydrocarbons C_2–C_6 are combined into

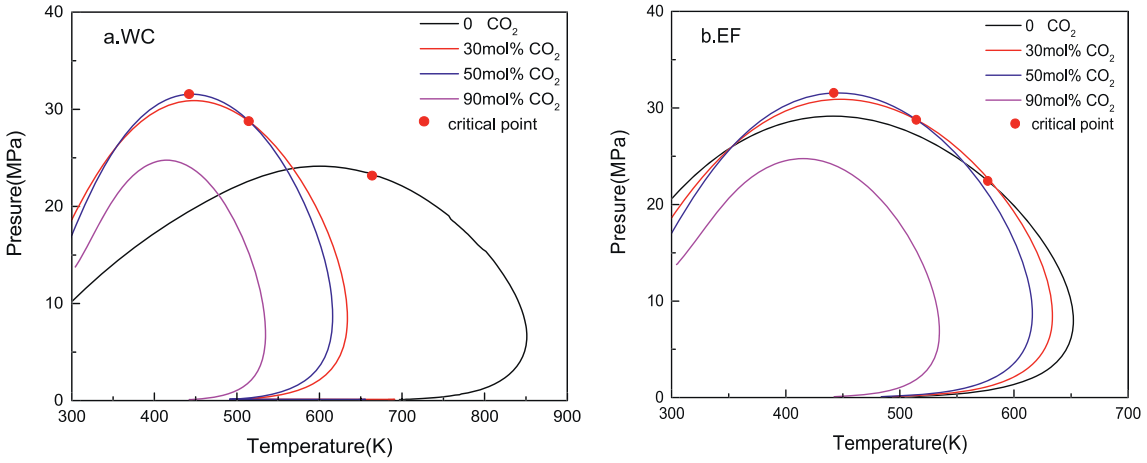


Fig. 5. Effect of CO_2 content on P-T phase diagram of WC and EF shale oils.

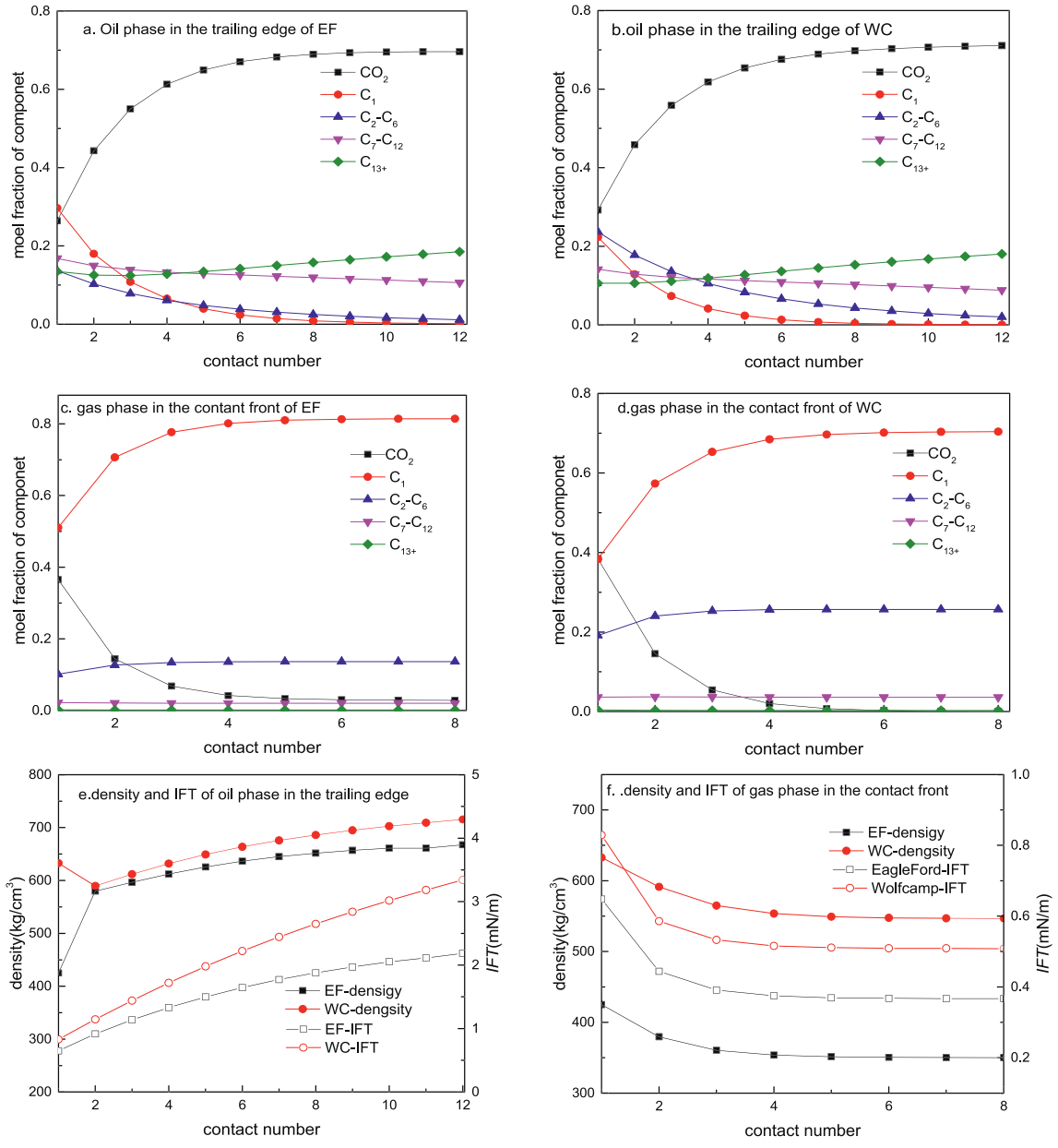


Fig. 6. Changes in fluid composition, density, and IFT during multiple contacts for EF and WC shale oils.

one item, and C_{13+} is combined into one item. A total of five proposed fractions are divided.

As shown in Fig. 6, CO_2 exhibits a strong extraction and dissolution ability, and the five components at the front and trailing edges of the EF and WC shale oils present similar change laws. As the number of contacts increases, the CO_2 content of the oil phase at the trailing edge of the contact increases quickly. In contrast, the methane content decreases rapidly, and the content of intermediate hydrocarbons C_2–C_{12} decreases. After the 4th contact round, the heavy hydrocarbon C_{13+} content begins to increase gradually. The continued CO_2 injection increases the gas-liquid composition differences at the trailing edge of the back-forward contact, raising the IFT (Fig. 6e).

It can also be observed from Fig. 6e that the density of the EF shale oil phase increases during the backward contact, while the density of the WC shale's oil phase decreases and then rises. The increase in density is mainly due to the decrease in C_1 and C_2–C_6 content in the oil phase. As the number of contacts increases, the CO_2 content in the vapor phase at the front of the forward contact decreases rapidly. In contrast, the methane content increases rapidly, and the intermediate hydrocarbons C_2–C_6 also increase. However, the changes in the C_7–C_{12} and C_{13+} contents are smaller. The continued CO_2 injection gradually decreases the gas-liquid composition differences at the front of the forward contact, reducing the IFT (Fig. 6c, d, and 6f). Therefore, CO_2 injection mainly supports forward-contact miscibility.

3.4. Phase behavior of fluid in nanopores

3.4.1. Bubble point pressure

For shale oil production, bubble point pressure (P_b) is a crucial factor. The P_b of EF shale oil (T = 389.26 K) and WC shale oil (T = 397.04 K) is investigated within the 2 nm–1000 nm range for pore radius (r_p), as shown in Fig. 7.

As shown in Fig. 7, P_b decreases with increasing r_p. When the r_p is less than 100 nm, P_b is suppressed. When the r_p is less than 20 nm, a significant change in P_b is observed. When $r_p = 10$ nm, the P_b of EF and WC shale oils decreased by 2.68 MPa (a 9.5% decrease rate) and 1.91 MPa (an 11.2% decrease rate), respectively. When $r_p = 3$ nm, P_b of EF and WC shale oils decreased by 6.60 MPa (a 23.5% decrease rate) and 4.29 MPa (a 25.2% decrease rate), respectively. This phenomenon delays the separation of the gas from the liquid phase, indicating that the gas remains dissolved in the liquid for an extended period. The light components in the oil reduce the viscosity and density of the shale oil in the nanopores, providing the oil with more energy to move from the nanopores to the natural fractures, thereby lowering the gas-oil ratio (GOR) and facilitating the production of shale oil.

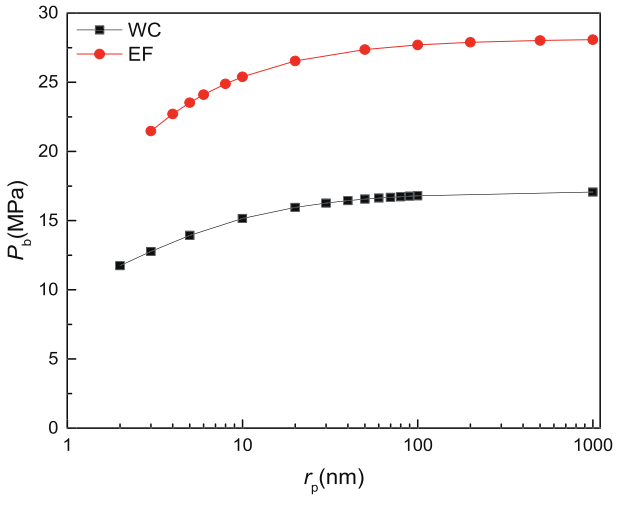


Fig. 7. Change curve for P_b of EF and WC shale oils and pore radius.

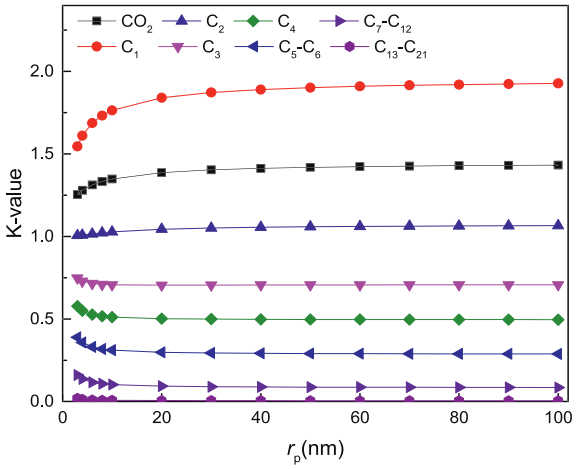


Fig. 8. K_i of EF shale oil at various pore radii.

3.4.2. Equilibrium constant value

Based on the VLE model, the values of equilibrium constants (K_i) for each component of EF shale oil (T = 389.26 K and P = 18.0 MPa) at different r_p are calculated, as shown in Fig. 8. As shown in Fig. 8, when the pore radius (r_p) is greater than or equal to 20 nm, the K_i of the components changes slightly with a decrease in r_p. When $r_p < 20$ nm, the values of the K_i of CO_2, C_1, and C_2 components significantly decrease with the r_p reduction, indicating the decrease of the gas-phase fraction of CO_2, C_1, and C_2 components. When $r_p < 6$ nm, the value of the K_i of the C_3–C_{21} component increased significantly, indicating that the vapor fraction of the C_3–C_{21} component increased. All the above phenomena increase the density of the gas phase, resulting in a corresponding decrease in the density of the liquid phases. As a result, the difference in density between the vapor and liquid phase is reduced. The main reason is that as the capillary pressure increases, the gas-phase pressure also increases, forcing components from the gas phase into the liquid phase. In addition, the nanoconfinement effect accelerates the mass transfer of components between the gas and liquid phases; the lighter the component, the greater the mass transfer.

3.4.3. Gas-liquid phase density

Fig. 9 depicts the changing rule of gas-liquid phase density for EF shale oil (T = 389.26 K and P = 16 MPa) and WC shale oil (T = 397.04 K and P = 10.342 MPa) at different pore radii (r_p). As seen in Fig. 9, for EF and WC shale oils, as the pore radius (r_p) decreases, the gas-phase density increases, the liquid density decreases, and the density difference between the vapor-liquid phases decreases. When the r_p is less than 20 nm, a more pronounced decrease in the liquid density can be observed. This phenomenon occurs because, under the nanoconfinement effect, the light components in the gas phase condense into the liquid phase, while the heavy components in the liquid phase evaporate into the gas phase. The more severe the nanoconfinement effect is, the more pronounced this phenomenon becomes. This phenomenon is consistent with the change in K_i value with pore size, as shown in Fig. 8. Thus, the IFT between the gas and oil phases decreases.

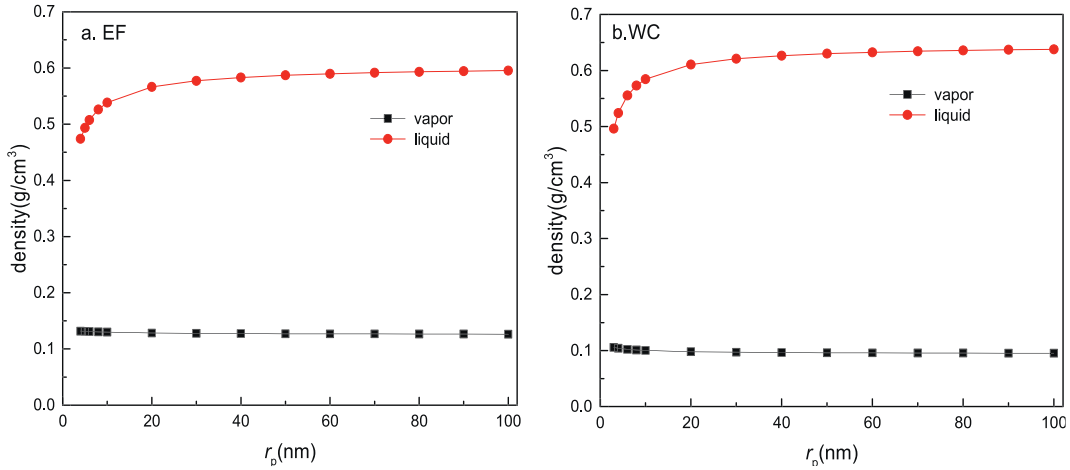


Fig. 9. Gas-liquid phase densities of EF and WC shale oils at different pore radii.

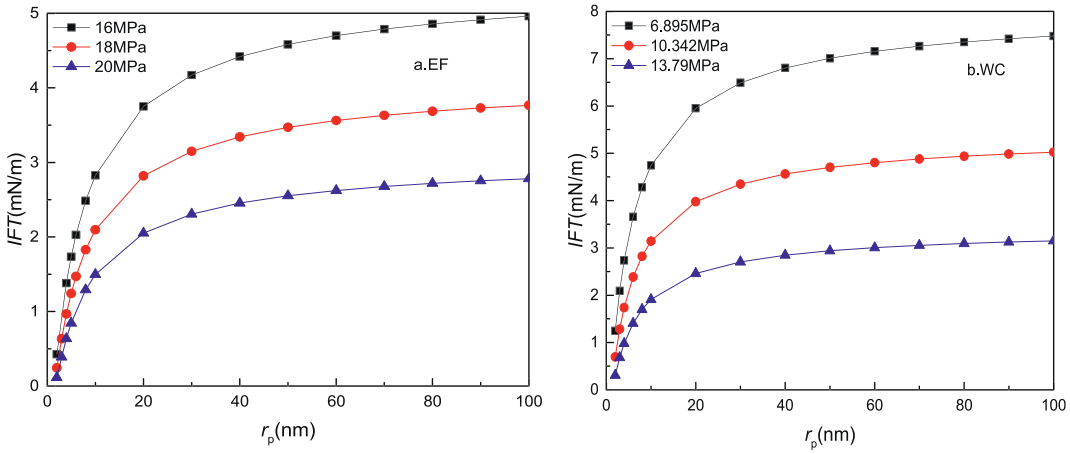


Fig. 10. EF and WC shale oil at different pore radii.

3.4.4. Gas-liquid interfacial tension and capillary forces

At the nano-scale, it is expected that the capillary force (P_{cap}) in nanopores will be extremely high. In this section, the impact of pore radius (r_p) on gas-liquid IFT and P_{cap} is investigated at different pressures. Fig. 10 depicts the variation rule of gas-liquid IFT with r_p for EF shale oil (T = 389.26 K) and WC shale oil (T = 397.04 K) at different pressures.

From Fig. 10, it can be observed that the IFT reduces slowly and then rapidly with decreasing pore radius (r_p), especially when the r_p is less than 20 nm. Under the same r_p, the IFT value is larger at

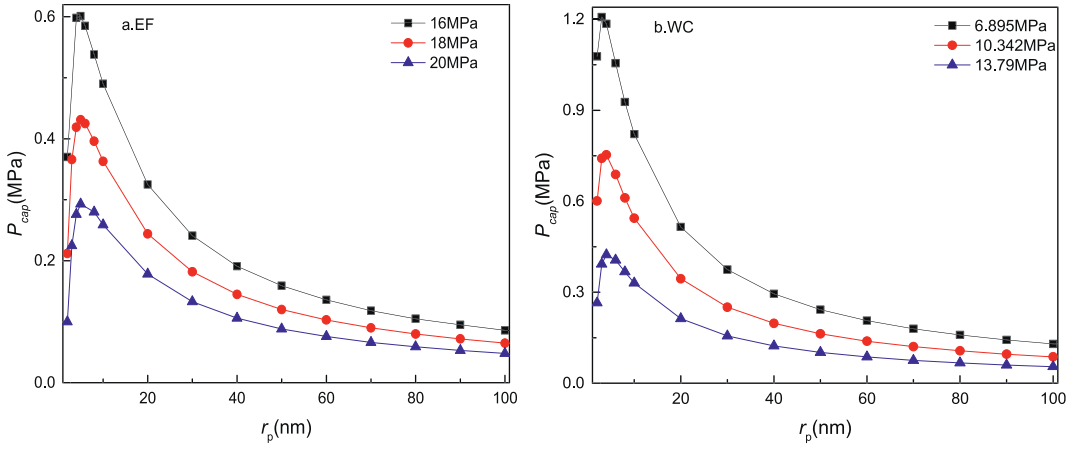


Fig. 11. P_{cap} of EF and WC shale oil at different pore radii.

low pressure. This phenomenon is mainly due to the considerable intermolecular distance and weak intermolecular force at low pressure. As a result, larger IFT values occur due to the inactivity of fluid molecules and the weakness of interphase mass transfer at low pressure, leading to relatively high IFT values. As shown in Fig. 10, the higher the system pressure and the smaller the pore size, the lower the IFT of the gas-liquid, which is favorable for the occurrence of miscibility. Additionally, the variation of IFT with pore radius is greater at low pressures than at high pressures. Therefore, at low pressures, the nanoconfinement effect has a larger influence on IFT.

Fig. 11 shows the change of capillary force (P_{cap}) with pore radius at different pressures for EF shale oil (T = 389.26 K) and WC shale oil (T = 397.04 K). From Fig. 11, it is found that when the pore radius (r_p) falls within a specific range (e.g., less than 5 nm), P_{cap} decreases as the r_p reduces. The main reason is that IFT and r_p have opposite effects on $P_{cap.}$ The gas-liquid IFT decreases sharply when the r_p decreases slightly. Thus, at a smaller r_p, the P_{cap} becomes smaller according to the Young-Laplace equation. When the r_p is > 5 nm, P_{cap} decreases with increasing pore radius (>5 nm), which is in line with the trend observed in conventional reservoirs (Li and Sheng, 2017). The lower the pressure, the greater the P_{cap}.

4. Conclusions

In this study, Eagle Ford and Wolfcamp shale oils were taken as research objects to comprehensively investigate the rules of phase behavior and mass transfer of CO_2-shale oil systems in nanopores. The conclusions are as follows.

(1) After CO_2 injection, the saturation pressure of shale oil tends to increase first and then decrease, and a critical point is observed when CO_2 injection exceeds 74 mol%. Under the same amount of CO_2 injection, the Wolfcamp shale oil has a larger reduction in the molecular weight and viscosity, and a smaller impact on the expansion coefficient and density.
(2) During the multi-contact CO_2 injection, CO_2 exhibits a strong extraction and dissolution ability. As the number of contacts increase, C_1–C_{12} components in shale oil are extracted into the gas phase, with some heavy components C_{13+} entering the gas phase. This results in the reduction of density and interfacial tension (IFT) at the forward contact front edge of shale oil with CO_2 injection. Therefore, the injection of CO_2 can lead to forward-contact miscibility.
(3) Under the nanoconfinement effect, the light components in the gas phase condense into the liquid phase, reducing the vapor-liquid phase's density difference and lowering the IFT, which is favorable for the gas-oil miscibility. When the pore radius (r_p) is less than 20 nm, the nanoconfinement effect becomes significant. Therefore, it will be easier to achieve miscibility in smaller nanopores (r_p < 20 nm), which is beneficial for CO_2-EOR.
(4) As the pore radius (r_p) decreases, the IFT first reduces gradually and then sharply, while the capillary force (P_{cap}) first increases, which is in agreement with the trend observed in conventional reservoirs. The P_{cap} then decreases, and a turning point is observed when the pore radius is less than 5 nm.

CRediT authorship contribution statement

FuLin Yang: Writing – original draft, Software, Investigation, Funding acquisition. **YingYing Chen:** Writing – original draft, Investigation.

Data availability statements

The data utilized to support the study's findings are provided in the article.

Declaration of competing interest

The authors declare that there are no conflicts of interest regarding the publication of this paper.

Acknowledgements

This study received financial support from the National Natural Science Foundation of China (Grant no.22268001) and the Guangxi Provincial Natural Science Foundation (Grant no.2018JJA120001).

References

Abu, A.F.A., Datta, R., 1999. Theoretical study of vapor-liquid equilibrium inside capillary porous plates. Fluid Phase Equilib. 162 (1–2), 83–96. https://doi.org/10.1016/S0378-3812(99)00197-1.
Abudour, A.M., Mohammad, S.A., Robinson, Jr., R.L., Gasem, K.A.M., 2013. Volume-translated Peng-Robinson equation of state for liquid densities of diverse binary mixtures. Fluid Phase Equilib. 349, 37–55. https://doi.org/10.1016/j.fluid.2013.04.002.
Adamson, A.W., 1990. In: Physical Chemistry of Surfaces, fifth ed. John Wiley & Sons, New York.
Brusilovsky, A.I., 1992. Mathematical simulation of phase behavior of natural multicomponent systems at high pressures with an equation of state. SPE Res. Eng. 7, 117–122. https://doi.org/10.2118/20180-PA.
Dong, X., Xu, W., Liu, H., Chen, Z., Lu, N., 2023. Molecular insight into the oil displacement mechanism of CO_2 flooding in the nanopores of shale oil reservoir. Pet. Sci. 20, 3516–3529. https://doi.org/10.1016/j.petsci.2023.08.006.
Dordzie, G., Balhoff, M., 2025. A review of chemical methods and testing techniques for enhanced oil recovery in shale reservoirs. Fuel 394 (15), 135060. https://doi.org/10.1016/j.fuel.2025.135060.
Hamada, Y., Koga, K., Tanaka, H., 2007. Phase equilibria and interfacial tension of fluids confined in narrow pores. J. Chem. Phys. 127, 084908. https://doi.org/10.1063/1.2759926.
Li, L., Sheng, J.J., 2017. Nanopore confinement effects on phase behavior and capillary pressure in a Wolfcamp shale reservoir. J. Taiwan Inst. Chem. Eng. 78, 317–328. https://doi.org/10.1016/j.jtice.2017.06.024.
Li, J., Lang, Y., Li, B., Zhang, H., Zhang, J., Rahman, S.S., 2025. Molecular mechanism of supercritical CO_2 enhancing shale oil production by extraction characteristics. Langmuir 41 (17), 11147–11160. https://doi.org/10.1021/acs.langmuir.5c01010.
Liu, X., Zhang, D., 2019. A review of phase behavior simulation of hydrocarbons in confined space: implications for shale oil and shale gas. J. Nat. Gas Sci. Eng. 68, 102901. https://doi.org/10.1016/j.jngse.2019.102901.
Liu, B., Lei, X., Feng, D., Ahmadi, M., Wei, Z., Chen, Z., Jiang, L., 2025. Nanoconfinement effect on the miscible behaviors of CO_2/shale oil/surfactant systems in nanopores: implications for CO_2 sequestration and enhanced oil recovery. Sep. Purif. Technol. 356, 129826. https://doi.org/10.1016/j.seppur.2024.129826.
Luo, S., Jin, B., Lutkenhaus, J.L., Nasrabadi, H., 2019. A novel pore-size-dependent equation of state for modeling fluid phase behavior in nanopres. Fluid Phase Equibibr 498, 72–85. https://doi.org/10.1016/j.fluid.2019.06.009.
Ma, Y., Jin, L., Jamili, A., 2013. Modifying Van Der Waals equation of state to consider influence of confinement on phase behavior. In: SPE Annual Technical Conference and Exhibition. https://doi.org/10.2118/166476-MS.SPE-166476-MS.
Mohagheghian, E., Hassanzadeh, H., Chen, Z., 2020. Evaluation of shale-gas-phase behavior under Nanoconfinement in mutimechanistic flow. Ind. Eng. Chem. Res. 59 (33), 15048–15057. https://doi.org/10.1021/acs.iecr.0c02615.
Nojabaei, B., Johns, R.T., Chu, L., 2013. Effect of capillary pressure on phase behavior in tight rocks and shales. SPE Res. Eval. Eng. 16 (3), 281–289. https://doi.org/10.2118/159258-PA.
Rezaveisi, M., Sepehrnoori, K., Pope, G.A., Johns, R.T., 2018. Thermodynamic analysis of phase behavior at high capillary pressure. SPE J. 23 (6), 1977–1990. https://doi.org/10.2118/175135-PA.
Rui, Z., Deng, H., Hu, T., Sheng, G., Wilson, M., Dinoruk, B., Patil, S., 2025. A coupling mechanism analysis of CO_2 non-darcy flow in multi-scale reservoirs: a case study of the life-cycle process of fracturing-development in shale oil reservoirs. Pet. Sci. 22 (3), 1171–1199. https://doi.org/10.1016/j.petsci.2024.12.018.
Salahschoor, S., Fahes, M., Teodoriu, C., 2017. A review on the effect of confinement on phase behavior in tight formations. J. Nat. Gas Sci. Eng. 51, 89–103. https://doi.org/10.1016/j.jngse.2017.12.011.
Sandoval, D., Yan, W., Michelsen, M.L., Stenby, E.H., 2015. Phase envelop calculations for reservoir fluids in the presence of capillary pressure. In: SPE Annual Technical Conference and Exhibition. https://doi.org/10.2118/175110-MS.SPE-175110-MS.

Song, Z., Song, Y., Guo, J., Zhang, Z., Hou, J., 2020a. Adsorption induced critical shifts of confined fluids in shale nanopores. Chem. Eng. J. 385, 123837. https://doi.org/10.1016/j.cej.2019.123837.

Song, Y., Song, Z., Liu, Y., Guo, J., Bai, B., Hou, J., Bai, M., Song, K., 2020b. Phase behavior and minimum miscibility pressure of confined fluids in organic nanopores. In: SPE Improved Oil Recovery Conference. https://doi.org/10.2118/200449-MS.SPE-200449-MS.

Song, Y., Song, Z., Guo, J., Feng, D., Chang, X., 2021. Phase behavior and miscibility of CO_2-hydrocarbon mixtures in shale nanopores. Ind. Eng. Chem. Res. 60 (14), 5300–5309. https://doi.org/10.1021/acs.iecr.1c00717.

Song, Z., Deng, S., Han, X., Zhang, Y., Zhang, L., Li, B., Chen, Y., Li, P., 2024. Phase characteristics and muti-round interaction mechanism of CO_2 /hydrocarbon gas injection in Gulong shale oil. J. Chongqing Univ. Sci. Technol. (Nat. Sci. Ed.) 26 (4), 1–10. https://link.cnki.net/doi/10.19406/j.issn.2097-4531.2024.04.001.

Tan, S.P., Piri, M., 2017. Retrograde behavior revisited: implications for confined fluid phase equilibira in nanopores. Phys. Chem. Chem. Phys. 19 (29), 18890–18901. https://doi.org/10.1039/C7CP02446K.

Tan, S.P., Qiu, X., Dejam, M., Adidharma, H., 2019. Critical point of fluid confined in nanopores: experimental detection and measurement. J. Phys. Chem. C 123 (15), 9824–9830. https://doi.org/10.1021/acs.jpcc.9b00299.

Teklu, T.W., Alharthy, N., Kazemi, H., Yin, X., Graves, R.M., Alsumiti, A.M., 2014. Phase behavior and minimum miscibility pressure in nanopores. SPE Reserv. Eval. Eng. 17 (3), 396–403. https://doi.org/10.2118/168865-PA.

Wang, Z., Liu, T., Liu, S., Jia, C., Yao, Jun, Sun, H., Yang, Y., Zhang, L., Delshad, M., Sepehrnoori, K., Zhong, J., 2024. Adsorption effects on CO_2-oil minimum miscibility pressure in tight reservoirs. Energy 288 (1), 129815. https://doi.org/10.1016/j.energy.2023.129815.

Wei, B., Zhong, M., Zhao, J., Wang, D., Kadet, V., You, J., 2022. Prediction method for the minimum miscibility pressure of crude oil and natural gas in micro-nano confined space. Acta Pet. Sin. 43 (11), 1604–1613. https://link.cnki.net/urlid/11.2128.TE.20220922.1748.006.

Yang, G., Fan, Z., Li, X., 2019. Determination of confined fluid phase behavior using extended Peng-Robinson equation of state. Chem. Eng. J. 378, 122032. https://doi.org/10.1016/j.cej.2019.122032.

Zarragoicoechea, G., Kuz, V., 2004. Critical shift of a confined fluid in a nanopore. Fluid Phase Equilib. 220 (1), 7–9. https://doi.org/10.1016/j.fluid.2004.02.014.

Zhang, K., Jia, N., Li, S., 2017. Exploring the effects of four important factors on oil-CO_2 interfacial properties and miscibility in nanopores. RSC Adv. 7, 54164. https://doi.org/10.1039/c7ra10671h.

Zhang, K., Jia, N., Li, S., Liu, L., 2019. Static and dynamic behavior of CO_2 enhanced oil recovery in shale reservoirs: experimental nanofluidics and theoretical models with dual-scale nanopores. Appl. Energ. 255, 113752. https://doi.org/10.1016/j.apenergy.2019.113752.

Zhao, Y., Jin, Z., 2019. Hydrocarbon-Phase Behaviors in shale nanopore/fracture model: Multiscale, multicomponent, and multiphase. SPE J. 24 (6), 2526–2540. https://doi.org/10.2118/198908-PA.